Physics of the Solid State, 2025, Vol. 67, No. 3

14,08

Effect of submicron Ti-Ni-Ta-based surface alloy on the mechanical properties of the TiNi alloy before and after thermal cycling of the system [Ti-Ni-Ta-based surface alloy|TiNi-substrate]

© F.A. D'yachenko, D. Chepelev, V.V. Loban', L.L. Meisner

Institute of Strength Physics and Materials Science, Siberian Branch,
Russian Academy of Sciences,
Tomsk, Russia

E-mail: dfa@ispms.ru

Received March 6, 2025
Revised March 7, 2025
Accepted March 7, 2025

The dependencies of changes in the mechanical properties of the TiNi alloy with synthesized surface alloy based on the Ti-Ni-Ta system with a thickness of $< 1\,\mu$m were investigated in torsion tests. The synthesis was carried out by alternating the operations of deposition of a $Ti_{60}Ta_{40}$ (at.%) alloying film and liquid-phase mixing of the film/substrate system using a low-energy high-current electron-beam. It has been shown that the presence of the surface alloy results in the preservation of martensite shear stresses $\tau_M \approx 460$ MPa, an increase in the width of the stress hysteresis loop $\Delta\tau$ by ~ 25 MPa, and an improvement in the ability of the material to accumulate and recover superelastic strain γ_{SE} by ~ 0.2 % more than the values in TiNi samples without irradiation and alloying. It was found that reducing of the thickness of the surface alloy does not lead to an increase in the crack resistance of the synthesized surface layer. It was found that thermal cycling of the modified samples in the temperature range of $B2-B19'$ martensitic transformation leads to a change in the elastic-stress state in the [surface alloy|TiNi-substrate] system, resulting in a reduction of stresses τ_M by ~ 100 MPa, and an increase in the crack resistance of the synthesized surface layer.

Keywords: electron-beam synthesis, torsion tests, martensitic transformations, surface morphology.

DOI: 10.61011/PSS.2025.03.60889.45-25

1. Introduction

Titanium nickelide based alloys (TiNi alloys) having the shape memory effect and superelasticity (SME-SE), are used to manufacture miniature medical (endosurgical tools, vascular implants, and dental products, etc.) [1–6] and non-medical (actuators, temperature sensors, damping devices, etc.) [7–9] products. Key concerns over TiNi alloys are: 1) degradation of physical and mechanical [10] and corrosive [11] properties due to the accumulation of fatigue defects; 2) low radiopacity of miniature products made from these alloys [12] and 3) toxicity to human body [3,4,6].

To improve physical and mechanical properties, corrosion resistance, radiopacity and biocompatibility of TiNi alloys provided that inelastic properties (SME-SE) are maintained, adaptive thin-film electron-beam synthesis [13] is used to form multicomponent surface alloys (SA) [13–20] with desired chemical composition (based on three-component (Ti-Ni-Ta, Ti-Ni-Nb) [13–18] and four-component (Ti-Ni-Ta-Si, Ti-Ni-Nb-Si) [19,20] systems) and thickness ($\sim 1-2\,\mu$m). The SA synthesis method [13–20] includes repeated alternation of deposition of doping film with a particular composition ($Ti_{85-70-60}Me_{15-30-40}$ and $Ti_{60}Me_{30}Si_{10}$ (at.%), where Me: Ta, Nb) and thickness ($\sim 50-100$ nm) and liquid-phase mixing of film and substrate components using a wide-aperture (up to $\sim 10\,\text{cm}^2$) low-energy (≤ 30 keV) high-current (up to ~ 25 kA) pulsed electron-beam (LEHCEB) with an energy density to $\sim 2.5\,\text{J/cm}^2$, a pulse duration of $\sim 2-4\,\mu$s in a single vacuum cycle.

Studies [13–15] demonstrate the efficiency of the electron-beam synthesis of amorphous Ti-Ni-Ta-based SA with a thickness of $\sim 2\,\mu$m and pre-defined structural characteristics and properties. It is shown that the synthesized amorphous SA has a high capacity of use in miniature medical and nonmedical products as protective barrier layers on the surface of TiNi alloys due to physical and stress-strain properties (high strength and plasticity, mechanical compatibility with TiNi substrate [14,15]) and decreased concentration of nickel on the surface [13,14]. In [12,13], it is shown that Ta-doped TiNi wire samples, according to angiographic data, have ~ 2 times as high radiopacity as angiograms of holometallic samples. Recent studies [15] showed that $\sim 2\,\mu$m amorphous SA didn't exert any critical impact on the integral properties of a TiNi substrate during cyclic torsion test, but, on the contrary, improves inelastic properties of miniature TiNi product prototypes. Electron microscopy of surface [15] showed that this SA didn't peel off from the TiNi substrate after the mechanical test.

It is known that sizes of medical and non-medical miniature TiNi products vary from several hundreds of nanometers to tens of millimeters [3–6,8]. For millimetersize products, controlled surface modification and improvement of properties of surface layers with a thickness from ~ 100 nm to $\sim 1{-}5\,\mu$m make it possible to keep the volumetric structure and properties (including SME-SE) while modifying drastically the material properties in the surface adjacent layers [13–20]. In the cases when miniature TiNi products are smaller than ≤ 1 mm (e.g. endosurgical tools, vascular implants, dental products [1–6]), volumetric structure and properties of the substrate material will be to a great extent defined by the modified layer properties (hardness and plasticity, residual elastic stress level after irradiation). In this case, on the one hand, the material shall retain the necessary inelastic properties (SME-SE). On the other hand, physical, stress-strain and surface sensitive properties of the substrate material shall be improved. Therefore, a promising opportunity includes surface modification of miniature TiNi products (≤ 1 mm) and control of stress-strain properties of the substrate material by altering the amorphous SA thickness, i.e. synthesizing a $\leq 1\,\mu$m surface layer.

The second reason for decreasing the amorphous SA thickness is the findings obtained in [15]. It is shown that, after the cyclic torsion test (with 20 loading/unloading cycles, to the accumulated torsional strain $\gamma_{\max} \approx 4\,\%$, with torsion rate $\sim 4\,\%$/min), local microcracking areas were detected on the SA surface. According to the results of [21–23], formation of thin ($\leq 1\,\mu$m) amorphous metal films on the surface of functional (TiNi alloy [21]) and structural (stainless steel [22], Ti-6Al-4V alloy [23]) materials facilitates an increase in plasticity of the synthesized surface layer and fatigue characteristics (fatigue limit, critical stress to failure) of [coating/substrate] systems. The authors' study [17] shows that, after a bend test (to $\sim 2\,\%$ strain with a loading rate of ~ 0.5 mm/min), any surface layer discontinuities (cracking or peel of SA from the TiNi substrate) were not detected on the surface of amorphous Ti-Ni-Ta ($\leq 1\,\mu$m) SA [16].

Thus, taking into account the findings of [16,17,21–23], there is reason to suggest the impact of the scale factor on the properties of the [SA|TiNi substrate] system, i.e. reduction of the amorphous SA thickness can facilitate 1) the improvement of the properties of miniature products (with thickness ≤ 1 mm) without critical impact on inelastic properties of the TiNi-substrate (SME-SE), and 2) the increase in fracture resistance of the [SA|TiNi-substrate] system.

It is known [6,9,24] that miniature TiNi products are thermomechanically cycled before operation to achieve stabilized thermomechanical and inelastic properties. For this, it is sufficient to carry out cycling with a set of ~ 10 to ~ 20 cycles [24] to achieve the best thermomechanical and inelastic properties in the last cycles for material operation.

In [25–27] it is shown that irreversible plastic strain can accumulate during thermal cycling (TC) of TiNi alloys with increasing number of cycles in the material and induce degradation of inelastic properties (SME-SE), including material performance impairment. One of the simplest thermal cycling techniques is a scheme at the martensitic transformation temperature intervals B2$-$B19$'$, which is defined as repetition of the „cooling below the direct martensitic transformation completion temperature M_f — heating above the inverse martensitic transformation completion temperature A_f" cycle. In [26], it was found that thermal cycling of TiNi alloys in coarse-grained and ultra-fine-grained states can cause microstructural changes, for example, formation and reproduction of dislocations, internal stress variation in the material. Structural changes that occur during thermal cycling can affect the stress-strain properties of a material, including parameters characterizing SME-SE.

Previously in [13–20], the effect of SA on the stress-strain properties of the TiNi alloy after thermal cycling of [SA|TiNi-substrate] systems in the martensitic transformation temperature range B2$-$B19$'$ was not identified. It was not understood how the stress-strain properties of a [SA|TiNi-substrate] system vary after thermal cycling in torsion test conditions. There is no data on whether thermal cycling will affect SA discontinuity.

Within the continued study [15], the following issues are discussed in this work:

1) how the synthesized amorphous SA thickness variation will affect the [SA|TiNi substrate] system strain behavior during torsion test;

2) [SA|TiNi substrate] system behavior after thermal cycling was not identified, including the thermal cycling effect on the stress-strain properties and surface morphology of the [SA|TiNi-substrate] system.

The objective of the study was to perform torsion test of non-planar miniature product prototypes to establish stress-strain property behavior of the TiNi alloy with $\leq 1\,\mu$m amorphous Ti-Ni-Ta SA synthesized on its surface, in particular, to identify the [SA|TiNi-substrate] behavior after thermal cycling within the martensitic transformation temperature range B2$-$B19$'$.

2. Materials, processing and study methods

2.1. Materials and surface preparation methods

The study used TH-1 TiNi alloy made by the vacuum induction melting process in a graphite crucible furnace (MATEK-SPF, Russia). Chemical composition of the alloy: Ti (balance)-55.75 Ni-0.035 O-0.02 C-0.003 N-0.001 H (wt.%). The ratio Ti:Ni in the B2(TiNi) phase corresponded to 49 : 51 (at.%). Direct and inverse martensitic start (M_s, A_s) and finish (M_f, A_f) temperatures B2$\rightleftarrows$B19$'$: $M_s = 288 \pm 2$ K, $M_f = 268 \pm 2$ K, $A_s = 308 \pm 2$ K, $A_f = 313 \pm 2$ K.

Rectangular parallelepiped samples, $1 \times 1 \times 25$ mm were cut by electrical discharge sawing in water from an initial semi-finished plate. Sample surface was prepared step-by-step: (1) chemical etching, (2) vibromechanical treatment, (3) ultrasonic cleaning, (4) electrolytic polishing, (5) ultrasonic cleaning. Surface preparation conditions are described in detail in [15]. The samples prepared in such a way were marked as TiNi.

2.2. Additive thin-film electron-beam synthesis of the Ti-Ni-Ta surface alloy

The Ti-Ni-Ta SA was synthesized on the TiNi samples using the „RITM-SP" (Microsplav, Russia) modified automated system [28,29] in a single vacuum cycle. The rectangular samples were secured in a fixture in the process chamber such that to perform surface modification simultaneously for two sides. Samples were installed on a travelling work table, which was moved to perform film deposition operations and pulsed electron-beam liquid phase mixing with substrate in a single vacuum cycle. Then atmosphere inlet was performed, samples were turned over, and the remaining two sides were treated.

For smoothing and homogenization of the surface layer on the TiNi samples, low-energy high-current electron-beam pulsed (LEHCEB) treatment was used in surface melting conditions (electron-beam energy density $E_s = 2.5\,\mathrm{J/cm^2}$, number of treatment pulses $n = 10$, maximum electron energy $U = 21\,\mathrm{keV}$, pulse duration $\sim 2{-}3\,\mu\mathrm{s}$).

Then $\sim 100\,\mathrm{nm}$ $\mathrm{Ti_{60}Ta_{40}}$ (at.%) film was deposited on the TiNi samples by magnetron method simultaneously from two magnetrons by sputtering single-component pure Ti (99.95 wt.%) and Ta (99.95 wt.%) (Girmet, Russia) targets. Composition of the deposited film was monitored by energy dispersive spectroscopy (X-ACT silicon drift detector (Oxford Instruments, Great Britain)) using the LEO EVO 50 scanning electron microscope (SEM) (Zeiss, Germany) at an accelerating voltage of $U = 10\,\mathrm{kV}$. According to the measurements, the film composition met the calculated composition with an accuracy of ± 2 at.%. The film was almost free of carbon. Oxygen concentration in the film was not higher than several at.%.

Electron-beam liquid-phase mixing of the [Ti-Ta-film|TiNi-substrate] system was performed using LEHCEB at $E_s = 2\,\mathrm{J/cm^2}$, $n = 10$, $U = 17\,\mathrm{keV}$, pulse duration $\sim 2{-}3\,\mu\mathrm{s}$. The number of „deposition/melting" synthesis cycles was repeated twice. The TiNi substrate temperature was not higher than $\sim 473\,\mathrm{K}$ by the end of the synthesis. Using these conditions, the expected thickness of the synthesized Ti-Ni-Ta SA was $\sim 200\,\mathrm{nm}$. TiNi samples after SA synthesis on the surface are marked as TiNi-SA.

2.3. Thermal cycling of the [surface alloy |TiNi substrate] system

TiNi-SA samples were subjected to thermal cycling with the number of „heating/cooling", cycles equal to 20. Thermal cycling was performed by cooling in liquid nitrogen to 77.4 K followed by heating in boiling water to 373 K, which was, respectively, below and above the direct M_f and inverse A_f finish temperatures of martensitic transformations B2 $\rightleftarrows$ B19$'$. Holding time in the heated and cooled states was $\sim 30\,\mathrm{s}$. TiNi-SA samples after thermal cycling are marked as TiNi-SA-TC.

2.4. Torsion test

Torsion test was performed on the NDV-100 (Metrotest, Russia) test machine in accordance with GOST 3565-80 [30]. M-Text ASU software (Metrotest, Russia) was used to control the test machine and to plot strain curves. The effective length of the samples was $l \approx 18\,\mathrm{mm}$. Torsion was performed clockwise at $T \approx 298 \pm 1\,\mathrm{K}$. Before the test, one end of the sample was fixed together with a measuring transducer of force torque M, the second transducer was inserted into a sliding cartridge with a sensor of torsion angle φ secured on it. Loads applied to the samples were recorded using a strain-gauge transducer, the upper torque measurement limit for which was $\sim 10\,\mathrm{N\cdot m}$. Before testing, cross-section area of all samples was measured. In different loading conditions, at least 3 samples from each of the TiNi, TiNi-SA and TiNi-SA-TC groups were subjected to the torsion test.

Accumulated and recovered strain in torsion was recorded in a form of „force torque M — torsion angle φ" curves, which were replotted into the „shear stress τ — shear strain γ" curves (Figure 1).

Tangential stresses τ were calculated using equation [31]

$$\tau = \frac{M}{J} = \frac{M6}{d^3},$$

where M is the force torque, J is the moment of resistance, d is the arithmetic mean thickness of the sample.

Shear strain γ was determined using equation [31]

$$\gamma = \frac{\varphi\, d\, 0.5}{l\, 180^\circ/\pi} \cdot 100\,\%,$$

where φ is the torsion angle, l is the sample effective length.

2.4.1. Cyclic test. Test cycle included torsion of the sample at a constant rate of $\sim 4\,\%/\mathrm{min}$ up to $\gamma_{\max} \approx 4$. Then, the load was released to zero at the same rate of rotation in the opposite direction. The number of test cycles N was set to 20 because it is known [6,9,24] that the finished miniature TiNi products are thermomechanically cycled with ~ 10 to ~ 20 cycles and stabilized thermomechanical and inelastic properties are addressed in the last cycles. The following parameters were determined from the obtained experimental data (Figure 1, *a*):

1) τ_{M} — martensite shear stress,

2) $\Delta\tau$ — stress hysteresis loop,

3) γ_{SE} — superelastic (inelastic) strain accumulated during loading above the elastic strength $\gamma_{\mathrm{SE}(1-2)}$ and reversible during unloading $\gamma_{\mathrm{SE}(3-4)}$,

4) γ_{res} — total residual strain accumulated after each test cycle.

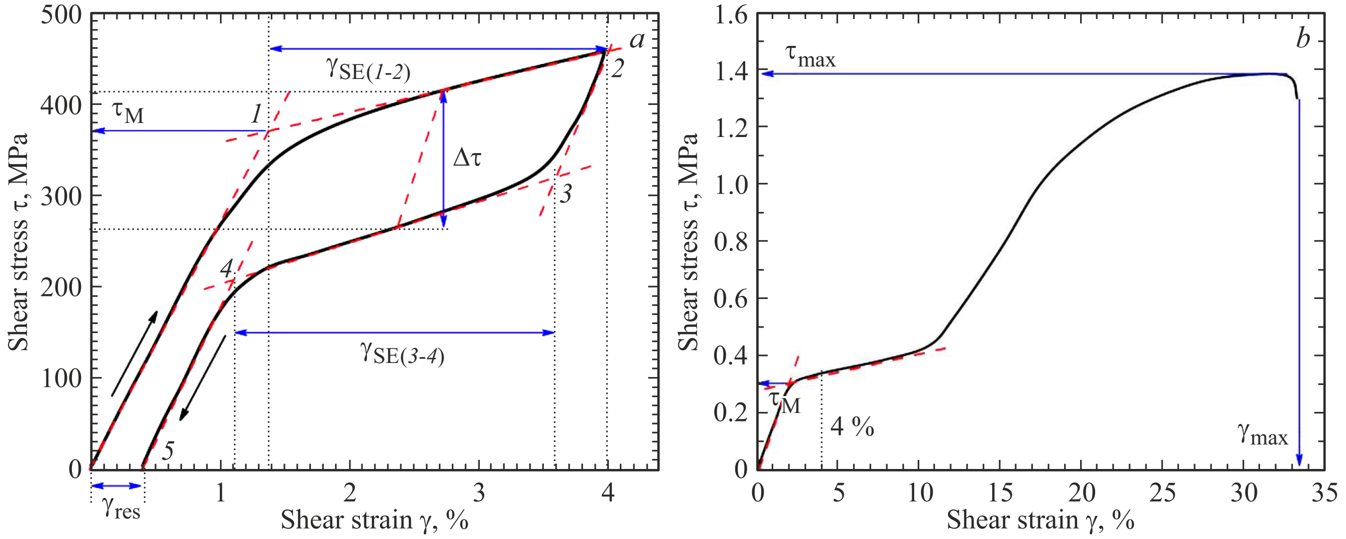

Figure 1. Schematic view of the shear stress τ vs. shear strain γ: *a* — during cyclic test and *b* — test to failure.

Then dependences of these parameters on test cycle N were plotted.

2.4.2. Test to failure. The samples were twisted at a constant rate ~ 4%/min until their failure was recorded. After testing, the following parameters were determined (Figure 1, *b*):

1) τ_{M} — martensite shear stress,

2) $\tau_{\max}$ — shear fracture strength,

3) $\gamma_{\max}$ — fracture strain.

2.5. Electron microscopic analysis of the surface

Surface morphology of the samples was examined using the LEO EVO 50 (Zeiss, Germany) and Apreo 2S (Thermo Fisher Scientific, USA) microscopes in secondary and backscattered electron imaging conditions at the accelerating voltage $U = 10-20$ kV and current $I = 1.5-2$ nA.

The studies were carried out on the equipment of „NANOTECH“ Center of Equipment Sharing ISPMS SB RAS (Russia, Tomsk).

3. Results and discussion

According to the data of [16], the Ti-Ni-Ta SA formed in this work using the same conditions consists primarily of an amorphous structure and has a thickness of $< 1\,\mu$m. The average chemical composition of SA is described as $\mathrm{Ti}_{\sim 50}\mathrm{Ni}_{\sim 40}\mathrm{Ta}_{\sim 10}$ (at.%). A martensite sublayer with a thickness≤ 100 nm consisting of the B19′(TiNi) phase is located under the amorphous layer and borders on an undoped area of the TiNi substrate located in the heat affected zone. Variations of stress-strain properties in the TiNi-SA samples subjected to torsion test will be discussed below.

3.1. Effect of the submicron Ti-Ni-Ta surface alloy on the stress-strain properties of TiNi alloy in torsion test

3.1.1. Cyclic test. Figure 2 shows the „shear stress τ — shear strain γ“ curves measured during testing of the TiNi samples (Figure 2, *a*) and TiNi-SA samples (Figure 2, *b*).

It is shown that the strain accumulation and recovery curves are similar for both groups of samples and have a „flag-like“ shape with a narrow hysteresis typical of TiNi alloys with the superelasticity effect [3,4,15,20,24]: first, a linear stage of elastic strain accumulation in the B2(TiNi) phase is observed when the applied load is increased, then there is a platform where the inelastic strain γ_{SE} is accumulated at the martensitic strain accumulation start stress τ_{M} resulting from the martensitic transformation initiated by loading and increase in the volumetric fraction of the martensite phase. If the applied load is released within the accumulated inelastic strain, then the material will recover the inelastic and elastic strains accumulated during loading.

Figure 2, *a* shows that, during testing of the TiNi samples, the shape of curves $\tau(\gamma)$ at the linear elastic strain accumulation and recovery stages is repeated during accumulation of N from 1 to 20. At the inelastic strain accumulation and recovery stages, the shape of curves $\tau(\gamma)$ varies from the 1-st to the 10-th cycle, then stabilizes with N from ~ 10 to 20. Testing of the TiNi-SA samples showed that the synthesized SA affected the shape of curves $\tau(\gamma)$, which indicated the variation of stress-strain properties in these samples (Figure 2, *b*). Then, for the TiNi samples before and after the SA synthesis, the values of examined parameters are given in the 20-th cycle to evaluate the cyclic stability of mechanical and inelastic properties.

Figure 3, *a* shows the dependences of τ_{M} on N. It can be seen that, with accumulation of N from 1 to 20 in the

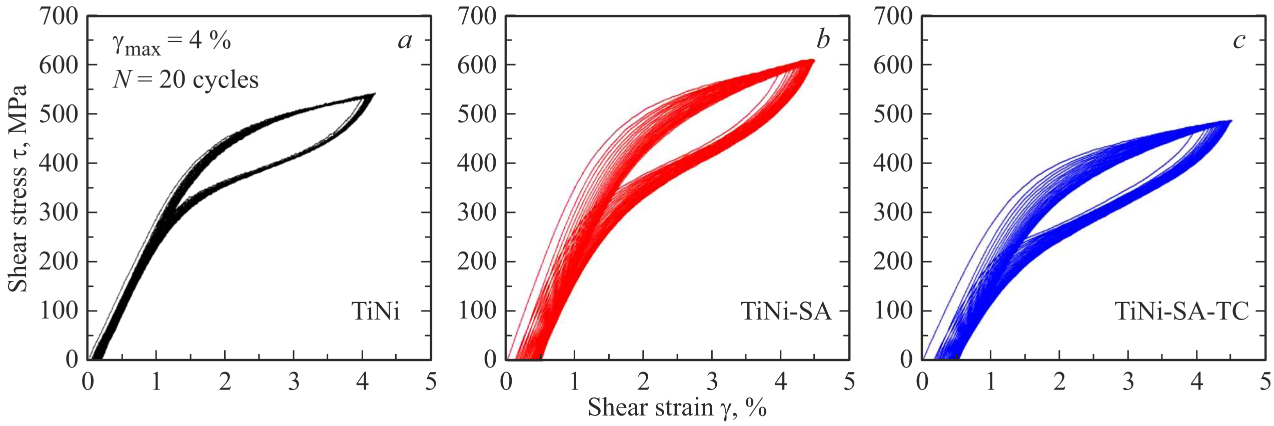

Figure 2. Dependences of shear stress τ on shear strain γ measured during cyclic torsion testing: *a* — TiNi, *b* — TiNi-SA and *c* — TiNi-SA-TC.

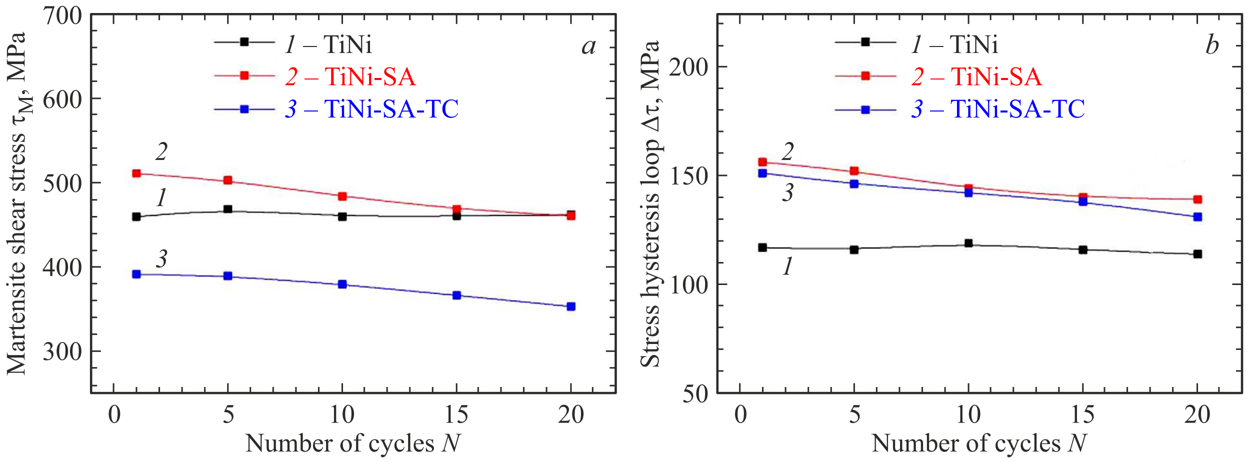

Figure 3. Martensite shear stress τ_M (*a*) and stress hysteresis loop $\Delta\tau$ (*b*) vs. the number of loading-unloading cycles N for samples: *1* — TiNi; *2* — TiNi-SA; *3* — TiNi-SA-TC.

TiNi and TiNi-SA samples, values of τ_M measured in the 20th cycle are the same between the samples and are equal to ~ 460 MPa (curves *1* and *2*). Increased values of τ_M in the TiNi-SA samples with accumulation of N from 1 to ~ 10 are caused by the fact that a higher force torque shall be applied to the modified samples at the torsional strain accumulation stages, which is probably associated with surface layer strengthening in these samples.

Figure 3, *b* shows $\Delta\tau$ vs. N. It was found that the mechanical hysteresis loop expanded by ~ 25 MPa in the TiNi-SA samples during accumulation of N from 1 to 20 (curves *1* and *2*). This might indicate that the presence of SA prevents from martensitic transformation reversibility.

Dependences of inelastic strain γ_{SE} accumulated in loading $\gamma_{\mathrm{SE}(1-2)}$ and recoverable in unloading $\gamma_{\mathrm{SE}(3-4)}$ on the number of loading/unloading cycles N are shown in Figure 4, *a* and *b*, respectively. It was found that $\gamma_{\mathrm{SE}(1-2)}$ and $\gamma_{\mathrm{SE}(3-4)}$ in the TiNi-SA samples were ~ 2.7 and ~ 2.5 %, respectively (curves *2*), which is higher by ~ 0.2 % than $\gamma_{\mathrm{SE}(1-2)}$ and $\gamma_{\mathrm{SE}(3-4)}$ in the TiNi samples (curves *1*). Increased time of inelastic strain γ_{SE} accumulation and recovery stages on curves $\tau(\gamma)$ may be attributed to the fact that as a result of higher torque applied to the hardened TiNi-SA samples a large volumetric fraction of the TiNi substrate material was involved in the TiNi-SA samples during γ_{SE} accumulation and recovery, reversible martensitic transformation $\mathrm{B2} \rightleftarrows \mathrm{B19'}$ took place in the substrate material giving rise to the growth of fractions of the accumulated $\gamma_{\mathrm{SE}(1-2)}$ and recovered $\gamma_{\mathrm{SE}(3-4)}$ torsional strains.

Figure 5 shows γ_{res} vs. N. It can be seen that SA affects the increase in the ability to accumulate γ_{res} by the TiNi alloy. Thus, when 20 cycles are accumulated in the TiNi and TiNi-SA samples, γ_{res} is equal to ~ 0.17 and ~ 0.48 %, respectively (curves *1* and *2*). After the test, strain nonrecovery with accumulation of N from 1 to 20 observed in the TiNi samples is caused by the presence of some residual fraction of martensite phase that can exist in the TiNi alloy with this composition at $T \approx 298$ K. In the TiNi-SA samples, regardless of the fact that the

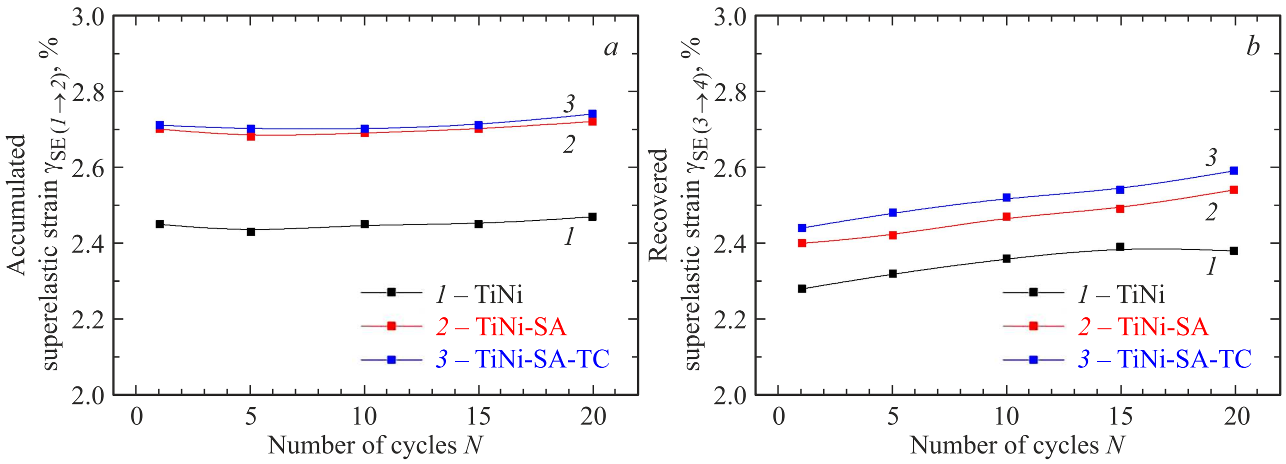

Figure 4. Superelastic (inelastic) strain γ_{SE} accumulated in loading $\gamma_{SE(1-2)}$ (a) and recoverable in unloading $\gamma_{SE(3-4)}$ (b) vs. the number of loading/unloading cycles N for samples: *1* — TiNi, *2* — TiNi-SA and *3* — TiNi-SA-TC.

fractions of the accumulated $\gamma_{SE(1-2)}$ and recovered $\gamma_{SE(3-4)}$ torsional strains have increased, increase in γ_{res} is associated with irreversible processes that occurred at a micro-scale level. As will be shown below during SEM image analysis, increase in $\Delta\tau$ and γ_{res} is associated with cracking of the TiNi-SA sample surface. Nevertheless, further heating of the TiNi-SA samples to $T \approx 308 \pm 1$ K leads to a decrease in γ_{res}, which is allowable for biomedical application of the TiNi alloy [1–6].

Thus, it follows from the analysis of dependences in Figures 2–5 that, regardless of a small thickness of amorphous SA ($\leq 1\,\mu$m), SA effect on the TiNi substrate is significant, and the patterns of parameter variations depending on N are similar, as during testing of the $\sim 2\,\mu$m amorphous SA [15].

3.1.2. Test to failure. Figure 6 shows the „shear stress τ — shear strain γ“ curves measured during testing of the TiNi samples (curve 1) and TiNi-SA samples (curve 2). As can be seen, curves $\tau(\gamma)$ during testing to failure have a typical form for materials exposed to martensitic transformations [4,10,26]: as the applied load is increased, a linear stage of elastic strain accumulation in the B2(TiNi) phase is first observed, then there is a martensitic yield platform at τ_M where γ_{SE} is accumulated as a result of martensitic transformation. As the load increases, a linear stage occurs and characterizes the elastic strain accumulation of the martensite phase. Then, there is a platform at which the material starts accumulating the plastic strain and finally failure occurs.

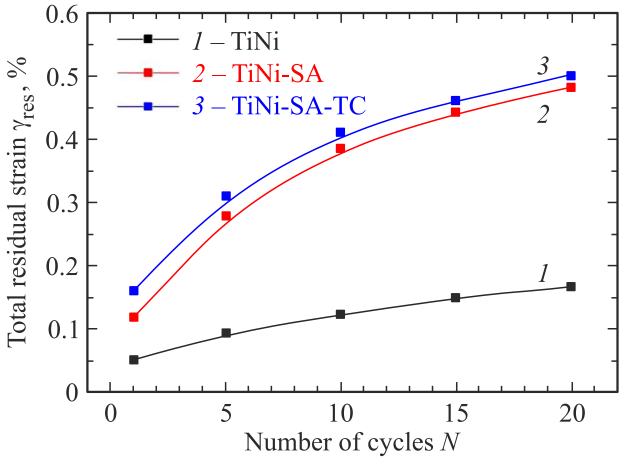

Figure 5. Dependences of total residual strain γ_{res} accumulated after each test cycle taking into account previous cycles on the number of loading/unloading cycles N for samples: *1* — TiNi, *2* — TiNi-SA and *3* — TiNi-SA-TC.

Figure 6 shows that the presence of SA didn't affect the shape of curve $\tau(\gamma)$. This means that the strain behavior of the TiNi-SA samples was not subjected to any change at all strain accumulation stages. However, as for the cyclic test, the presence of SA on the TiNi sample surface leads to the increase in τ_M. During strain accumulation $\gamma \geq 4\,\%$ in the TiNi-SA samples, high τ is maintained on the martensitic yield platform compared with that of the TiNi samples. Torsional strength τ_{max} in the TiNi-SA samples is ~ 2.22 GPa, which is ~ 150 MPa as high as τ_{max} in the TiNi, for which $\tau_{max} \approx 2.07$ GPa. Increase in τ_{max} in the TiNi-SA samples is probably associated with the fact that the synthesized layer doesn't undergo severe cracking or peel of from the substrate material during testing to failure, therefore, its effect is maintained at all strain accumulation stages until failure. Note that accumulation of the maximum strain to failure γ_{max} in the TiNi-SA samples is $\sim 63\,\%$, which is close to that in the TiNi samples, for which $\gamma_{max} \approx 60\,\%$. This means that the presence of SA on the TiNi alloy surface doesn't suppress the material capability to accumulate plastic strain.

Thus, analysis of dependences in Figure 6 shows that the presence $< 1\,\mu$m amorphous SA on the TiNi alloy surface results in the growth of τ_{max} to ~ 2.22 GPa without affecting

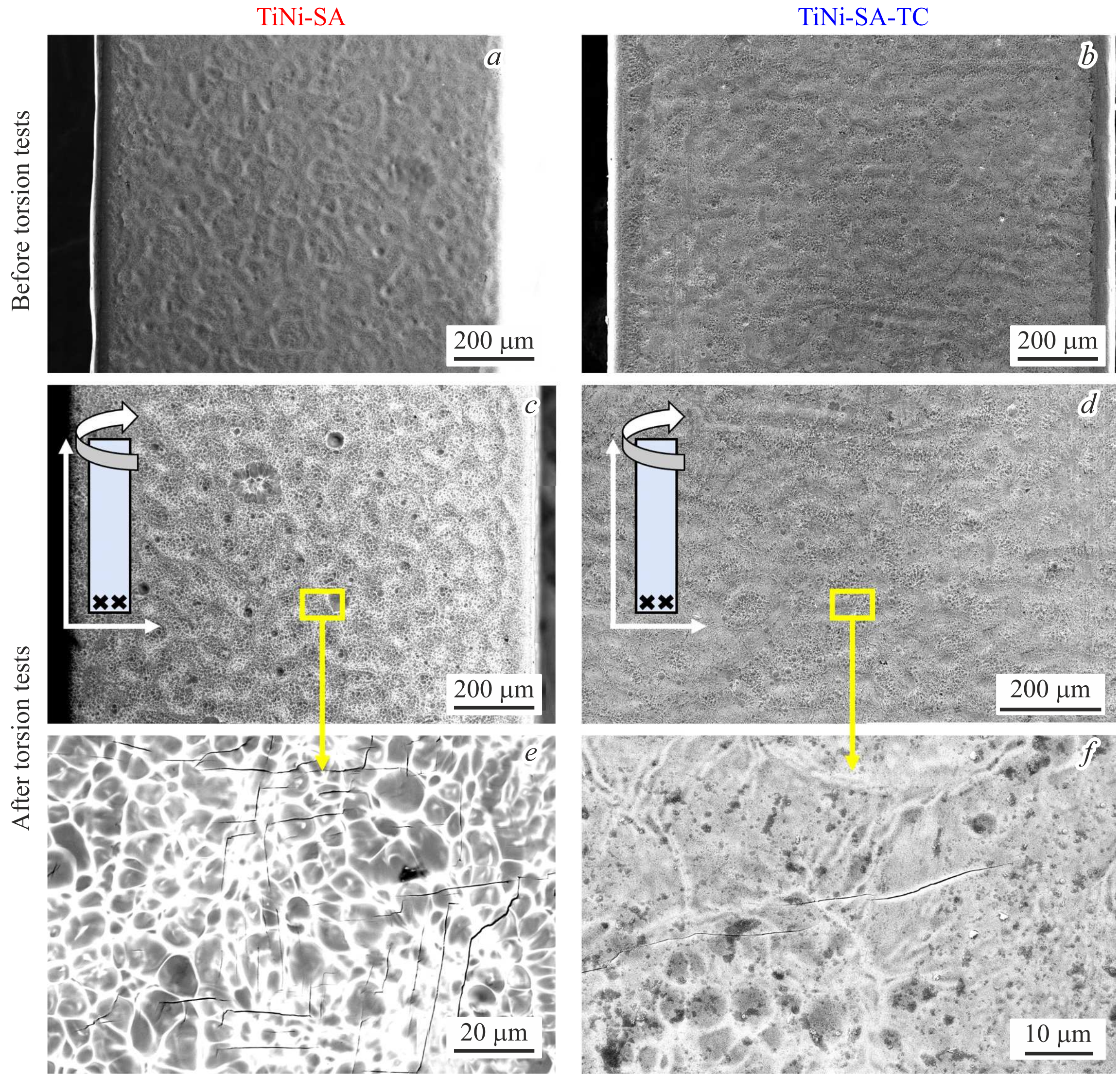

Figure 7. SEM images of the sample surface before (*a, b*) and after (*c–f*) the cyclic torsion test ($\gamma_{\max} = 4\,\%$, $N = 20$, $T = 298 \pm 1\,\mathrm{K}$) of samples: *a, c, e* — TiNi-SA; *b, d, f* — TiNi-SA-TC.

the material capability to accumulate $\gamma_{\max}$ that is equal to $\sim 63\,\%$.

3.2. Electron microscopy examinations of the submicron Ti-Ni-Ta surface alloy morphology after the cyclic torsion test

To study the SA discontinuity, cleavage and crack analysis and search for areas with delamination of SA from the substrate material were performed after cyclic torsion testing. SEM examination data for the TiNi samples without irradiation and doping are provided in [15]. It is shown that the TiNi surface prepared by means of machining and electrochemical treatment is homogeneous and is free from any cleavage or cracking after cyclic testing. Figure 7 shows SEM-images of the TiNi-SA surface before (Figure 7, *a*) and after (Figure 7, *c* and *e*) the cyclic torsion test.

After synthesizing the $< 1\,\mu$m SA, the TiNi-SA surface has homogeneous morphology on all sides, without macroscopic SA discontinuities (cracking or peel of) (Figure 7, *a*). After the cyclic testing, it was found that the TiNi-SA surface at all sides was homogeneous and there were also no signs of SA delamination from the TiNi substrate (Figure 7, *c*). However, as for the samples with $\sim 2\,\mu$m amorphous SA [15], similar local microcracking areas occurred on the sample surfaces in this case (Figure 7, *e*). Microcracks are oriented longitudinally and laterally with respect to the axis of torsion of the sample, occur only on the sides of the effective length and don't approach the edges.

Thus, as can be seen from the data shown in Figure 7, *c* and *e*, the decrease in the amorphous SA thickness doesn't contribute to an increase in the fracture resistance of the [SA|TiNi substrate] system. A positive result is in that

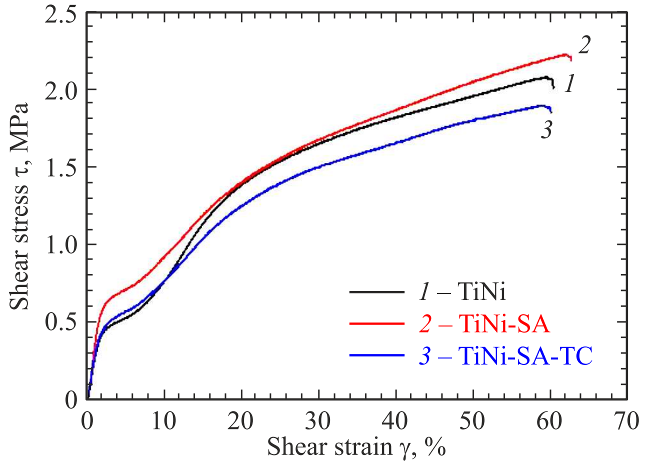

Figure 6. Dependences of shear stress τ on shear strain γ measured during torsion testing to failure: *1* — TiNi, *2* — TiNi-SA and *3* — TiNi-SA-TC.

the $\leq 1\,\mu$m amorphous SA doesn't peel of from the TiNi substrate.

3.3. Thermal cycling effect on the deformation behavior of the [surface alloy|TiNi substrate] system during the torsion test

Regardless of the fact that the decreasing SA thickness didn't contribute to any increase in the [SA|TiNi substrate] fracture resistance, the thermal cycling test gave a positive effect. Thermal cycling effect on the mechanical properties and surface morphology of the TiNi-SA-TC samples will be discussed below.

3.3.1. Mechanical properties of the [surface alloy |TiNi substrate] system after thermal cycling. Figure 2, *c* shows that thermal cycling of the TiNi-SA-TC samples didn't alter the strain behavior of the TiNi alloy, however, had the most significant effect on τ_M.

It was found that τ_M decreased to ~ 355 MPa in the 20th cycle in the TiNi-SA-TC samples (Figure 3, *a*, curve *3*). It is shown that thermal cycling caused the decrease in τ_M by ~ 100 MPa compared with that in the TiNi-SA samples. However, the temperature change virtually didn't affect the behavior of $\Delta\tau(N)$, $\gamma_{SE}(N)$ and $\gamma_{res}(N)$, and the measurements in the 20th cycle are as follows $\Delta\tau \approx 131$ MPa, $\gamma_{SE(1-2)} \approx 2.7\,\%$, $\gamma_{SE(3-4)} \approx 2.5\,\%$ and $\gamma_{res} \approx 0.5\,\%$ (Figure 3–5, curves *3*), which corresponds to those for the TiNi-SA samples.

A decrease in stresses was also found in the TiNi-SA-TC samples during torsion to failure (Figure 6, curve *3*). It is shown that τ_{max} after thermal cycling is ~ 1.89 GPa, which is lower than that for the TiNi samples by ~ 180 MPa. The thermal cycling effect on the capability of material to accumulate γ_{max} remains unchanged and is equal to $\sim 60\,\%$. In our opinion, the decrease in stresses induced by thermal cycling might be attributed to the following structural changes:

1) due to formation, accumulation and stabilization of defects [25–27]. However, reduction of stresses in the TiNi-SA-TC samples most probably has nothing to do with this fact. In [26], it was shown that defect accumulation in the multiple martensitic transformation process during thermal cycling affects the increase in strength of TiNi alloys;

2) it is known [16,18] that electron-beam treatments form residual elastic stress fields that may give rise not only to formation of martensite sublayers in the heat affected zone [13,14,16,19,20], but also affect the elastic stress of near-surface layers, including the change of microhardness H and modulus of elasticity E [13,14,18–20]. One of the possible reasons for reduction of stresses in the TiNi-SA-TC samples is in that thermal cycling caused the alteration of elastic stress of the [SA|TiNi substrate] system, in particular, affected the relaxation of residual elastic stress fields in the near-surface layers, which in turn made the material more compliant to the applied torsional force.

It is planned to review the stress reduction mechanisms in the [SA|TiNi substrate] system before and after thermal cycling in separate studies of surface layer structure and residual elastic stress level in the surface layers.

3.3.2. [Surface morphology of [surface alloy|TiNi substrate] system after thermal cycling. Figure 7 shows SEM-images of the TiNi-SA-TC surface before (Figure 7, *b*) and after (Figure 7, *d* and *f*) the cyclic torsion test. After thermal cycling, the TiNi-SA-TC surface morphology is homogeneous on all sides, free from macroscopic SA discontinuities. This result means that the $\leq 1\,\mu$m amorphous SA doesn't undergo any cracking or delamination during thermal cycling of the [SA|TiNi substrate] system in the martensitic transformation temperature range B2–B19′. Taking into account that finished miniature TiNi products are themomechanically cycled before operation [6,9,24], this result shows that the synthesized SA meets the surface layer integrity requirements.

After the cyclic testing, the surface of all TiNi-SA-TC sides is homogeneous and there are no signs of SA peel off from the TiNi substrate (Figure 7, *d*). Review of high-magnification SEM images showed that single local microcracking areas occurred on the sample surfaces (Figure 7, *f*), but the number of microcracks was less that on the surface of TiNi-SA samples (Figure 7, *e*). The SA discontinuity areas are located in the center of the effective length of the samples and don't approach the edges. Microcracks are oriented longitudinally and laterally relative to the axis of torsion of the sample.

In the TiNi-SA-TC samples, lower microcracking is associated with the decrease in τ_M compared with that in the TiNi-SA samples (Figure 3, *a*, curves *2* and *3*). In other words, a lower torque applied to the TiNi-SA-TC samples gave rise to a less number of microcracks.

These results show that, regardless of the fact that the amorphous SA thickness reduction didn't contribute to any increase in the [SA|TiNi substrate] fracture resistance, additional thermal cycling treatment reduce surface microcracking. Taking into account that the problem of low adhesive stability of amorphous thin films causes delamination of the films from the substrate material [22,23], the [SA|TiNi substrate] system after thermal cycling demonstrates a positive result.

4. Conclusion

The additive thin-film electron-beam method with a doping $Ti_{60}Ta_{40}$ (at.%) film applied to the surface of TiNi samples in the form of rectangular parallelepipeds was used to synthesize amorphous Ti-Ni-Ta surface alloy with a thickness $< 1\,\mu$m. Thermal cycling of the [SA|TiNi substrate] system was performed in the martensitic transformation temperature range $B2-B19'$. Effect of the submicron SA on the mechanical properties of TiNi alloy during the torsion test was examined. It was shown that SA had no critical effect on the integral properties of TiNi substrate, but, on the contrary, improved inelastic properties of the miniature TiNi product prototypes. Using the torsion test and scanning-electron microscopy data, the following conclusions were made.

1) Electron-beam synthesis of the amorphous Ti-Ni-Ta SA with a thickness $\leq 1\,\mu$m was found to cause the increase in the width of mechanical hysteresis of stresses $\Delta\tau$ by ~ 25 MPa and the improvement of the capability of material to accumulate and recover inelastic strain γ_{SE} higher by $\sim 0.2\,\%$ than that of the TiNi samples. The martensitic strain accumulation start stresses τ_M measured in the 20 th cycle remain unchanged and are equal to ~ 460 MPa.

2) Regardless of a small SA thickness ($\leq 1\,\mu$m), the presence of SA on the TiNi alloy surface leads to the growth of τ_{max} to ~ 2.22 GPa without affecting the material capability to accumulate γ_{max} that is equal to $\sim 63\,\%$.

3) Electron microscopy examinations showed that the submicron amorphous SA didn't peel off from the TiNi substrate after the cyclic torsion test. However, the decrease in the SA thickness didn't contribute to any increase in the [SA|TiNi substrate] fracture resistance.

4) Thermal cycling of the [SA|TiNi substrate] within the martensitic transformation temperature range $B2-B19'$ affected a) the reduction of τ_M by ~ 100 MPa leading to b) the increase in the fracture resistance of the [SA|TiNi substrate] system.

Thus, for medical and non-medical miniature (≤ 1 mm) products made of TiNi alloys, in order to improve the mechanical properties, radiopacity, corrosion resistance and biocompatibility by synthesizing the Ti-Ni-Ta surface alloys, additional thermal cycling treatment serve as a tool to change the elastic stress of the [SA|TiNi substrate] system facilitating increased fracture resistance of the synthesized surface layer.

Funding

The work was funded by Russian Science Foundation No. 24-72-00017, https://rscf.ru/en/project/24-72-00017/.

Conflict of interest

The authors declare no conflict of interest.

References

[1] W. Abd-Elaziem, M.A. Darwish, A. Hamada, W.M. Daoush. Mater. Des. **241**, 112850 (2024). https://doi.org/10.1016/j.matdes.2024.112850

[2] R. Sarvari, P. Keyhanvar, S. Agbolaghi, M.S. Gholami Farashah, A. Sadrhaghighi, M. Nouri, L. Roshangar. Int. J. Polym. Mater. Polym. Biomater. **71**, *5*, 315 (2020). https://doi.org/10.1080/00914037.2020.1833010

[3] N. Sabahi, W. Chen, C.-H. Wang, J.J. Kruzic, X. Li. JOM **72**, *3*, 1229 (2020). https://doi.org/10.1007/s11837-020-04013-x

[4] J. Zhu, Q. Zeng, T. Fu. Corros. Rev. **37**, *6*, 539 (2019). https://doi.org/10.1515/corrrev-2018-0104

[5] U. Roshan, R. Amarasinghe, N. Dayananda. J. Rob. Networking Artif. Life **5**, *3*, 194 (2018).

[6] J.M. Jani, M. Leary, A. Subic, M.A. Gibson. Mater. Des. **56**, 1078 (2014). https://doi.org/10.1016/j.matdes.2013.11.084

[7] R. Braga, P. Freitas Rodrigues, H. Cordeiro, P. Carreira, M.T. Vieira. Mater. **15**, *14*, 4787 (2022). https://doi.org/10.3390/ma15144787

[8] M. Mehrpouya, H. Cheraghi Bidsorkhi. Micro Nanosyst. **8**, *2*, 79 (2016). https://doi.org/10.2174/1876402908666161102151453

[9] A. Nespoli, S. Besseghini, S. Pittaccio, E. Villa, S. Viscuso. Sens. Actuators A **158**, *1*, 149 (2010). https://doi.org/10.1016/j.sna.2009.12.020

[10] V.S. Kalashnikov, V.V. Koledov, V.G. Shavrov, V.A. Andreev, A.V. Nesolenov, D.S. Kuchin, R.D. Karelin. J. Commun. Technol. Electron. **68**, *4*, 400 (2023). https://doi.org/10.1134/S1064226923040046

[11] F. Sun, L. Jordan, V. Albin, V. Lair, A. Ringuede, F. Prima. ACS Omega **5**, *6*, 3073 (2020). https://doi.org/10.1021/acsomega.9b04312

[12] E.Yu. Gudimova, L.L. Meisner, S.N. Meisner, O.I. Shabalina, A.A. Boshchenko, A.E. Baev, S.I. Vintizenko. Tech. Phys. **65**, *4*, 645 (2020). https://doi.org/10.1134/S1063784220040088
Patent № 13(2017137653/15) RF, MPK A61L 065731, B82B 27/06, C22C 1/00, A61L 45/10, C22C 31/18, C23C 45/04. Sposob sinteza rengenokontrastnogo poverkhnostnogo Ti-Ta-Ni splava s amorphnoj ili amorfo-nanokristallicheskoj strukturoj na podlozhke iz TiNi splava. L.L. Meisner, A.B. Markov, G.E. Ozur, V.P. Rotshtein, S.N. Meisner, E.V. Yakovlev, E.Yu. Gudimova, V.O. Semin, Patentoobladatel' IFPM SO RAN, ISE SO RAN. Publ. 11.04.18. (in Russian).

[14] F.A. D'yachenko, V.O. Semin, M.G. Ostapenko, L.L. Meisner. Phys. Solid State **65**, *4*, 593 (2023). https://doi.org/10.21883/PSS.2023.04.56000.24

[15] F.A. D'yachenko, V.V. Loban', V.O. Semin, D.V. Chepelev, M.G. Ostapenko, L.L. Meisner. Phys. Solid State **66**, 1193 (2024).

[16] M.G. Ostapenko, V.O. Semin, L.L. Meisner, F.A. D'yachenko, S.N. Meisner, E.M. Oks, K.P. Savkin, A.B. Markov, E.V. Yakovlev, S.I. Yuzhakova, D.V. Chepelev, V.V. Loban'. Russ. Phys. J. **66**, *5*, 503 (2023). https://doi.org/10.1007/s11182-023-02968-3

[17] F.A. D'yachenko, D.V. Chepelev, L.L. Meisner. Springer Proceed. Phys. **412**, 55 (2024). https://doi.org/10.1007/978-981-97-1872-6_9

[18] L.L. Meisner, V.P. Rotshtein, V.O. Semin, A.B. Markov, E.V. Yakovlev, S.N. Meisner, D.A. Shepel, A.A. Neiman, E.Yu. Gudimova, F.A. D'yachenko, R.R. Mukhamedova. Mater. Charact. **166**, 110455 (2020). https://doi.org/10.1016/j.matchar.2020.110455

[19] F.A. D'yachenko, V.O. Semin, A.R. Shugurov, M.G. Ostapenko, L.L. Meisner. Surf. Coat. Technol. **474**, 130123 (2023). https://doi.org/10.1016/j.surfcoat.2023.130123

[20] F.A. D'yachenko, V.O. Semin, M.G. Ostapenko, L.L. Meisner, A.B. Markov, E.V. Yakovlev. Russ. Phys. J. **66**, *12*, 1287 (2024). https://doi.org/10.1007/s11182-023-03074-0

[21] C.-W. Chi, Y.-L. Deng, J.-W. Lee, C.-P. Lin. J. Formosan Med. Associat. **116**, *5*, 373 (2017). https://doi.org/10.1016/j.jfma.2016.07.003

[22] H. Jia, F. Liu, Z. An, W. Li, G. Wang, J.P. Chu, J.S.C. Jang, Y. Gao, P.K. Liaw. Thin Solid Films **561**, 2 (2014). https://doi.org/10.1016/j.tsf.2013.12.024

[23] C.M. Lee, J.P. Chu, W.Z. Chang, J.W. Lee, J.S.C. Jang, P.K. Liaw. Thin Solid Films **561**, 33 (2014). https://doi.org/10.1016/j.tsf.2013.08.027

[24] H. Tobushi, A. Ikai, S. Yamada, K. Tanaka, C. Lexcellent. J. Physique IV France **06**, *C1*, 385 (1996). https://doi.org/10.1051/jp4:1996137

[25] S.P. Belyaev, N.N. Resnina, K.O. Anshukova. Tech. Phys. Lett. **39**, *3*, 284 (2013).

[26] A.A. Tchurakova, D.V. Gunderov, A.V. Lukyanov, Yu.A. Lebedev. Lett. Mater. **3**, *2*, 166 (2013). https://doi.org/10.22226/2410-3535-2013-2-166-168

[27] H. Tobushi, K. Date, K. Miyamoto. J. Solid Mech. Mater. Eng. **4**, *7*, 1094 (2010). https://doi.org/10.1299/jmmp.4.1094

[28] G.E. Ozur, D.I. Proskurovsky. Plasma Phys. Rep. **44**, *1*, 18 (2018). https://doi.org/10.1134/S1063780X18010130

[29] A.B. Markov, A.V. Mikov, G.E. Ozur, A.G. Padei. Instrum. Exp. Tech. **54**, *6*, 862 (2011). https://doi.org/10.1134/S0020441211050149

[30] GOST 3565–80 Metally. Metod ispytaniya na kruchenie. Izd-vo standartov (1980) 17 s. (in Russian).

[31] A. Bhaduri. Mechanical Properties and Working of Metals and Alloys. Springer Singapore, Singapore. (2018), 748 p. https://doi.org/10.1007/978-981-10-7209-3

Translated by E.Ilinskaya